

Polarization-Insensitive, Orthogonal Linearly Polarized and Orthogonal Circularly Polarized Synthetic Aperture Metalenses

Jijian Hu * , Zhenghong Dong, Xuanwen Yang, Lurui Xia, Xueqi Chen and Yan Lu

School of Space Information, Space Engineering University, Beijing 101416, China

* Correspondence: yuanfang202201@163.com

Abstract: Metalenses have attracted much attention from researchers because they are thin, multifunctional and easy to integrate. However, due to the limitation of fabrication techniques and the influence of working wavelength, it is difficult to realize a large aperture. In this paper, we design and simulate polarization-insensitive, orthogonal linearly polarized and orthogonal circularly polarized synthetic aperture metalenses. We use a synthetic aperture to improve the cutoff frequency of the metalens and achieve an equivalent large-aperture metalens. We compare the modulation transfer function and focusing efficiency of synthetic aperture metalenses with different array structures. This work provides an effective solution to the needs of large-aperture metalenses, and metalenses with different polarizations can play an important role in polarization imaging.

Keywords: synthetic aperture metalens; polarization; modulation transfer function; focusing efficiency



Citation: Hu, J.; Dong, Z.; Yang, X.; Xia, L.; Chen, X.; Lu, Y. Polarization-Insensitive, Orthogonal Linearly Polarized and Orthogonal Circularly Polarized Synthetic Aperture Metalenses. *Photonics* **2023**, *10*, 348. <https://doi.org/10.3390/photronics10040348>

Received: 12 February 2023

Revised: 8 March 2023

Accepted: 19 March 2023

Published: 23 March 2023



Copyright: © 2023 by the authors. Licensee MDPI, Basel, Switzerland. This article is an open access article distributed under the terms and conditions of the Creative Commons Attribution (CC BY) license (<https://creativecommons.org/licenses/by/4.0/>).

1. Introduction

Metasurfaces are composed of special subwavelength nanostructures arranged according to specific laws, which have a powerful ability to regulate the amplitude, phase and polarization of electromagnetic waves [1,2]. Therefore, metasurfaces have a wide range of applications, including metalenses [3–6], beam controllers [7], holograms [8,9] and so on. As an important application of metasurfaces, metalenses are attracting much attention from researchers because they are thin, multifunctional and easy to integrate [10–14]. At present, common metalens fabrication techniques include electron beam lithography [15], nanoimprint lithography [16], projection lithography [17], two-photon lithography [18], etc. Due to the limitation of fabrication techniques and the influence of working wavelength, it is difficult to achieve a large aperture. Recently, Junwei Li et al. reported a long-wavelength infrared metalens with a diameter of 80 mm, which is the largest-known-aperture metalens [19]. However, this is still not enough to meet the demand for large-diameter metalenses.

The synthetic aperture metalens (SAM) is an effective method to solve the above problem [20]. A synthetic aperture is a series of easy-to-manufacture small-aperture systems combined into a large-aperture optical system to achieve the high-resolution requirements of the large-aperture system [21,22]. SAM is composed of several small-aperture metalenses, which can synthesize signals of multiple subapertures to improve the cutoff frequency of the metalens and obtain the equivalent large-aperture metalens.

Polarization is one of the important characteristics of light, and the information contained in it can be used to analyze the shape, surface roughness, texture and physical and chemical properties of materials [23], etc. Polarization imaging can obtain both the traditional imaging information of the target and the polarization information, which can be used to achieve the functions of defogging, image enhancement and three-dimensional reconstruction [24–27], etc. Because of its powerful capability, polarization imaging is widely used in industrial detection, biosensing, remote sensing and military fields, etc.

Because the metalens can simultaneously acquire multiple polarizations on a single chip [28,29], and it is thin, multifunctional and easy to integrate, the polarization imaging

system using metalenses is more miniaturized and integrated than the traditional system. The reported SAMs are polarization-insensitive. In order to expand the application of SAMs in polarization imaging, this paper designs and simulates the polarization-insensitive, orthogonal linearly polarized and orthogonal circularly polarized SAMs. We study Golay3, Cross and Annulus type SAMs, and compare the modulation transfer function (MTF) and focusing efficiency of SAMs with different array structures and filling factors. We use a synthetic aperture to improve the cutoff frequency of the metalens and achieve an equivalent large-aperture metalens.

2. Materials and Methods

2.1. Design of Metalens

Metalenses usually consist of periodic arrangement of subwavelength elements, which can flexibly adjust the amplitude, phase and polarization of light by changing the element geometry, rotation angle, resonance mode and other parameters. The commonly used phase control principles of metalenses include propagation phase and Pancharatnam–Berry phase (P-B phase) [30]. The design of metalenses generally includes the following three steps: (1) establishing the unit cell library (UCL) according to the materials; (2) establishing the metalens model according to the phase distribution; (3) simulating and calculating the performance parameters. In this paper, the working wavelength of the metalens is 12 μm . The unit cell consists of the Si nanorods ($n = 3.411$) and the BaF2 ($n = 1.386$) substrate, and the side length of the lattice is 6 μm . The FDTD software is used for EM simulation. The light sources used in the simulation are plane light sources. For the simulation of unit cell, periodic boundaries are used in x and y axis, and PML is used in z axis. For the simulation of metalens, the x , y and z axis all use PML.

2.1.1. Design of the Polarization-Insensitive Metalens

The unit cell of polarization-insensitive metalens (PIM) is a highly symmetrical cylinder in the x - y plane. The height and radius of the nanorods can be adjusted to regulate the propagation phase. The FDTD software is used to establish the periodic cell structure model and carry out parameter sweeping. The sweeping results are shown in Figure 1c,d. In order to achieve high focusing efficiency, we select the height of the nanorods with high transmittance and gentle variation and the propagation phase variation covers $0\sim 2\pi$. Based on the sweeping results, the height of the nanorods can be determined to 8 μm . Then, according to the relationship between the radius of the nanorods and the propagation phase, the UCL is determined by dividing $0\sim 2\pi$ into 8 intervals, as shown in Table 1.

The ideal phase distribution of the PIM is as follows:

$$\varphi(x, y) = -\frac{2\pi}{\lambda}(\sqrt{x^2 + y^2 + f^2} - f) \quad (1)$$

where $\varphi(x, y)$ represents the phase of any point on the metalens, λ is the free space working wavelength and f is the focal length of the metalens.

According to the ideal phase distribution formula, a PIM simulation model is established in FDTD software by using the UCL above. The diameter of the metalens is set to 150 μm and the focal length to 150 μm . The normalized distribution of the square of the electric field intensity of the metalens is shown in Figure 2. Integrating the electric field to calculate the focusing efficiency, which is the ratio of the energy in three times of the full width at half maximum (FWHM) range with the focal point as the center to the total incident energy. By calculation, the focusing efficiency of the PIM is 68%.

2.1.2. Design of the Orthogonal Linearly Polarized Metalens

Orthogonal linearly polarized metalenses (OLPM) can simultaneously focus two orthogonal linearly polarized lights separately in the same aperture. It can be used as a key component of orthogonal linear polarization imaging, which can be used for defogging and image enhancement. In order to focus the incident light of orthogonal linearly polarized

lights through an aperture to two different focal points, the metalens unit cells need to have different phase responses to different linearly polarized lights at the same time. Therefore, the focus of the OLPM design is to build a UCL that can simultaneously respond to different linearly polarized lights. The specific design process of the OLPM is as follows:

Firstly, the shape, period and height of the unit cell are determined. Because the nanorods have different responses to different linear polarization, and considering the fabrication difficulty, the rectangular nanorods are adopted. With reference to the sweeping results of the PIM elements, the period is set to $6\ \mu\text{m}$ and the height of the nanorods is set to $8\ \mu\text{m}$.

Secondly, establish the unit cell model and sweep parameters. The light sources of the simulation model are set as X-polarized light and Y-polarized light in turn. In the range of $1\sim 5\ \mu\text{m}$, the length and width of the rectangular nanorods are changed with the step size of $0.5\ \mu\text{m}$, and the changes of transmittance and propagation phase are recorded, as shown in Figure 3.

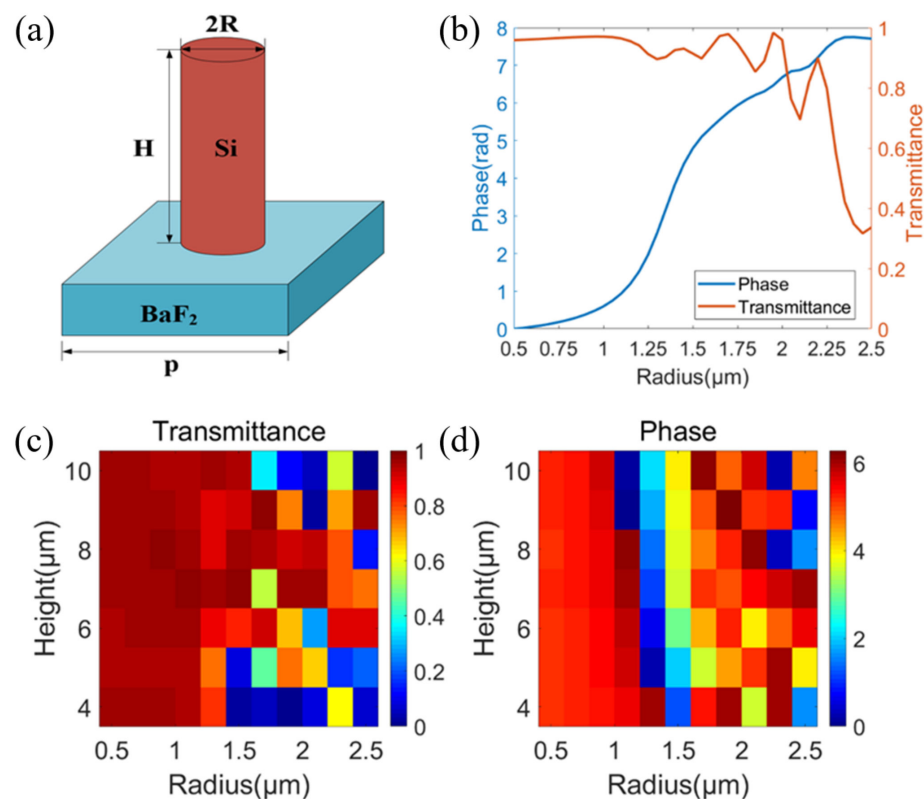


Figure 1. (a) Schematic of a unit cell of the PIM. (b) The transmittance and phase changes of the nanorods at $8\ \mu\text{m}$ height. (c) The relationship between the transmittance and the height and radius of the nanorods. (d) The relationship between the propagation phase and the height and radius of the nanorods.

Table 1. The UCL of the PIM.

Number	1	2	3	4	5	6	7	8
Phase (rad)	0	$\pi/4$	$\pi/2$	$3\pi/4$	π	$5\pi/4$	$3\pi/2$	$7\pi/4$
Transmittance	0.96	0.97	0.94	0.90	0.90	0.93	0.91	0.97
Radius (μm)	0.5	1.05	1.2	1.3	1.35	1.4	1.5	1.65

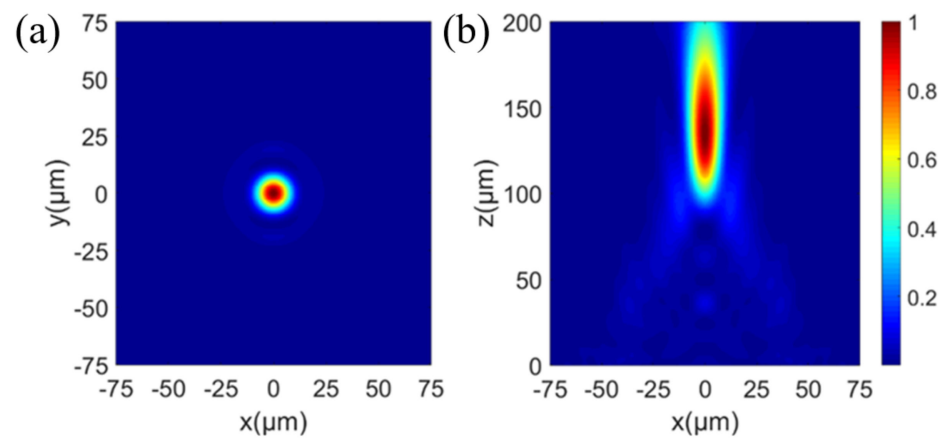


Figure 2. The normalized distribution of the square of the electric field intensity of the PIM: (a) X–Y plane; (b) X–Z plane.

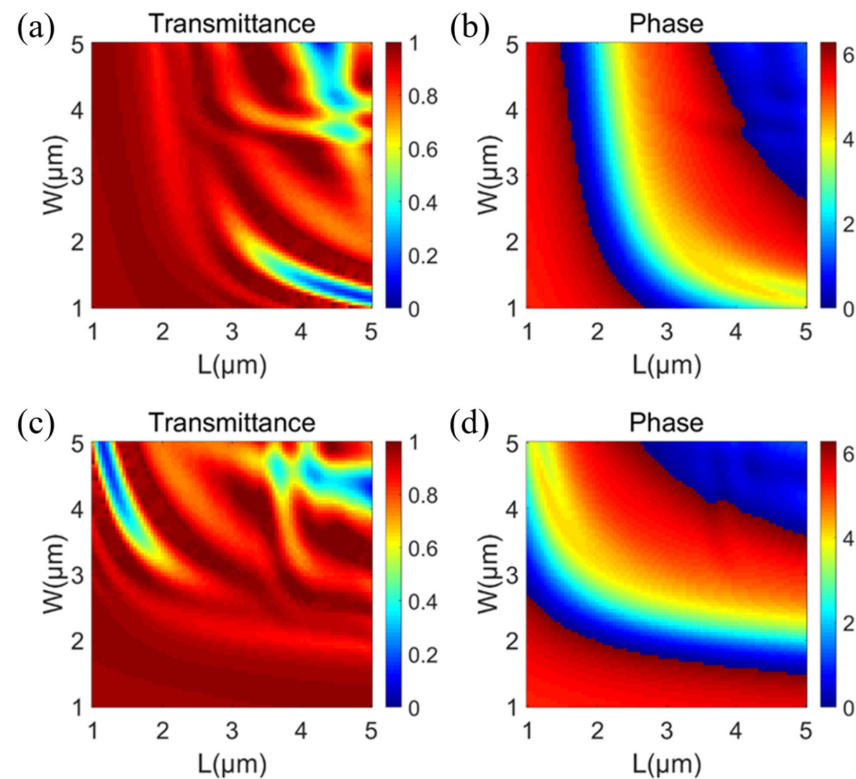


Figure 3. The relationship between the transmittance and the length and width of the nanorods: (a) X–polarized light; (c) Y–polarized light. The relationship between the propagation phase and the length and width of the nanorods: (b) X–polarized light; (d) Y–polarized light.

Then, the UCL is determined according to the different responses of the nanorods to X- and Y-polarized light. With reference to the PIM design, the UCL is determined by dividing $0\sim 2\pi$ into 8 intervals for one type of linearly polarized light, so that 64 basic unit-cell elements are required. In order to achieve high focusing efficiency of the metalens, the hierarchical screening method is used to search for the basic unit cell elements. Firstly, a search is conducted within the range of transmittance > 0.9 and phase error $< 22.5^\circ$; if there are no elements that meet the conditions, then the range of transmittance > 0.85 and phase error $< 22.5^\circ$ is searched; if the appropriate elements cannot be found, then the transmittance threshold is reduced appropriately until 64 basic unit cell elements are all determined.

If the X- and Y-polarized lights passing through the metalens are focused on the left and right sides of the Z-axis in the X-Z plane, then the ideal phase distributions of the OLPM are as follows:

$$\varphi_x(x, y) = -\frac{2\pi}{\lambda}(\sqrt{x^2 + 2xf \sin \alpha + y^2 + f^2} - f) \tag{2}$$

$$\varphi_y(x, y) = -\frac{2\pi}{\lambda}(\sqrt{x^2 - 2xf \sin \alpha + y^2 + f^2} - f) \tag{3}$$

where $\varphi_x(x, y)$ and $\varphi_y(x, y)$ represent the phase of X-polarized light and Y-polarized light at any point on the metalens, respectively. λ is the free space working wavelength, f is the focal length of the metalens and α is the off-axis angle of the focus. As can be seen from Equations (2) and (3), the focal points of X-polarized light and Y-polarized light are $(-f \sin \alpha, 0, f \cos \alpha)$ and $(f \sin \alpha, 0, f \cos \alpha)$, respectively.

Finally, the OLPM model is established and simulated. The diameter of the designed metalens is 150 μm , the focal length is 150 μm and the off-axis angle of the focus is 8° . The metalens light sources are set to X-polarized light, Y-polarized light and 45° polarized light in turn, and the normalized distributions of the square of the electric field intensity of the metalens are shown in Figure 4. The focusing efficiencies of X-polarized light and Y-polarized light are 67% and 66%, respectively. The extinction ratio between the two orthogonally polarized channels is 0.03 dB.

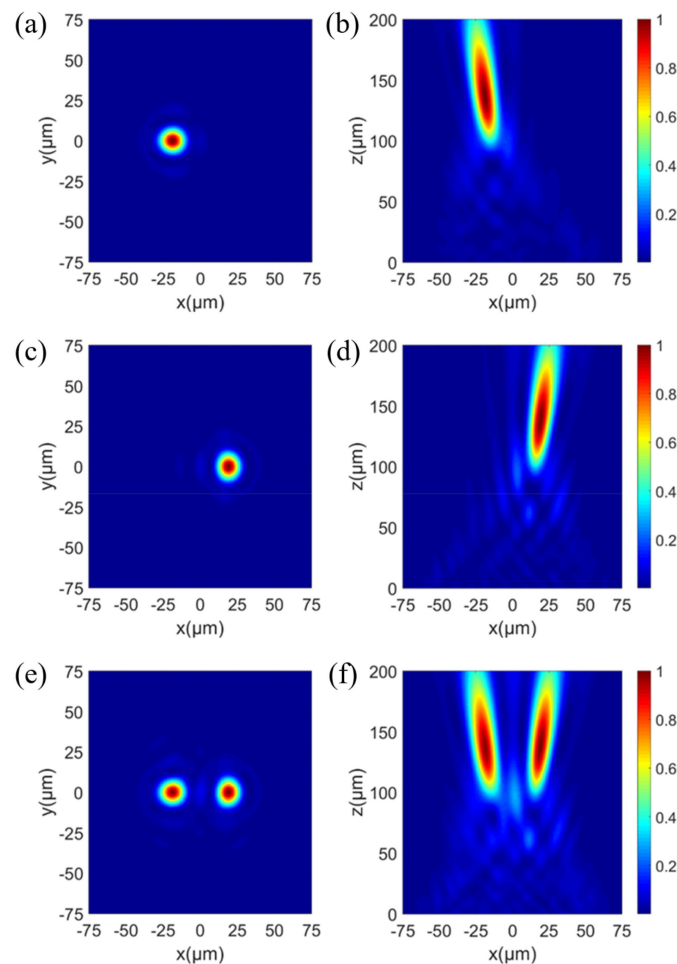


Figure 4. The normalized distribution of the square of the electric field intensity when X-polarized light, Y-polarized light and 45° polarized light successively pass through the OLPM: (a,c,e) X-Y plane; (b,d,f) X-Z plane.

2.1.3. Design of the Orthogonal Circularly Polarized Metalens

Circularly polarized light has the characteristics of memory, and it has great application potential in defogging and target recognition. The orthogonal circularly polarized metalens (OCPM) can simultaneously focus two orthogonal circularly polarized lights in the same aperture without the circular polarizer. Therefore, compared with the traditional circular polarization imaging, the OCPM has the advantages of miniaturization, integration and improving the light energy utilization efficiency.

P-B phase principle is often used for phase regulation of circularly polarized metalenses. Since P-B phase cannot simultaneously regulate two orthogonal circularly polarized lights, this paper uses the method of combining the propagation phase and P-B phase to regulate the phase of the OCPMs. When circularly polarized light passes through a unit cell, the transmitted light can be represented by the Jones vector as follows [31]:

$$\begin{bmatrix} E_{xout} \\ E_{yout} \end{bmatrix} = T \frac{1}{\sqrt{2}} \begin{bmatrix} 1 \\ ik \end{bmatrix} = \frac{1}{2\sqrt{2}} \left\{ (t_u + t_v) \begin{bmatrix} 1 \\ ik \end{bmatrix} + (t_u - t_v) e^{-2ik\theta} \begin{bmatrix} 1 \\ -ik \end{bmatrix} \right\} \quad (4)$$

where E_{xout} and E_{yout} are the electric field components of the transmitted light of in the X- and Y-axis directions, respectively. $k = \pm 1$, corresponding to the left-handed circularly polarized (LCP) light and right-handed circularly polarized (RCP) light, respectively. θ is the rotation angle of the nanorods.

If the LCP and RCP lights passing through the metalens are focused on the left and right sides of the Z-axis in the X-Z plane, then the ideal phase distributions of the OCPM are as follows:

$$\varphi_{LCP}(x, y) = -\frac{2\pi}{\lambda} (\sqrt{x^2 + 2xf \sin \alpha + y^2 + f^2} - f) \quad (5)$$

$$\varphi_{RCP}(x, y) = -\frac{2\pi}{\lambda} (\sqrt{x^2 - 2xf \sin \alpha + y^2 + f^2} - f) \quad (6)$$

where $\varphi_{LCP}(x, y)$ and $\varphi_{RCP}(x, y)$, respectively, represent the phase of LCP and RCP light at any point on the metalens; λ is the free space working wavelength; f is the focal length of the metalens; and α is the off-axis angle of the focus. According to the Equations (5) and (6), the focal points of LCP and RCP lights are $(-f \sin \alpha, 0, f \cos \alpha)$ and $(f \sin \alpha, 0, f \cos \alpha)$, respectively.

Suppose that φ_p is the propagation phase of the nanorods and θ is the rotation angle of the nanorods. In order to realize the phase regulation of the OCPM, φ_p and θ are as follows:

$$\varphi_p = \frac{\varphi_{LCP} + \varphi_{RCP}}{2}; \theta = \frac{\varphi_{LCP} - \varphi_{RCP}}{4} \quad (7)$$

The specific design process of the OCPM is as follows:

Firstly, the shape, period and height of the unit cell are determined. Like the OLPM, the nanorods are rectangular, and the period is 6 μm and the height of the nanorods is 8 μm . In order to simplify the design process, the transmittance, propagation phase and conversion rate of LCP and RCP lights are calculated by using the sweeping results of X- and Y-polarized lights. The conversion rate is defined as the ratio of the energy of the circularly polarized light orthogonal to the incident light to the total energy. When the RCP light is incident, the output LCP and RCP lights can be obtained by the following formula:

$$E_{LCPout} = E_{xout} - E_{yout}; E_{RCPout} = E_{xout} + E_{yout} \quad (8)$$

where E_{xout} and E_{yout} are the electric field components of the transmitted light in the X- and Y-axis directions, respectively, and E_{LCPout} and E_{RCPout} are the output electric fields of LCP and RCP lights, respectively.

Then, the UCL is determined according to the response results of the unit cells. It can be seen from the above analysis that the phase regulation of the metalens is completed by both the propagation phase and the P-B phase. The propagation phase is realized by changing the structural parameters of the nanorods, and the P-B phase is realized by

changing the rotation angle of the nanorods. Therefore, we determine the UCL according to the propagation phase. Like the OLPM, the hierarchical screening method is used to search for the 8 basic unit cell elements. Figure 5c,d are the transmission and the propagation phase distribution of the unit cells meeting the conditions of transmittance > 0.9 and conversion rate > 0.9, respectively. According to the results of Figure 5d, the 8 basic unit cell elements can be screened out and the result is shown in Figure 5e.

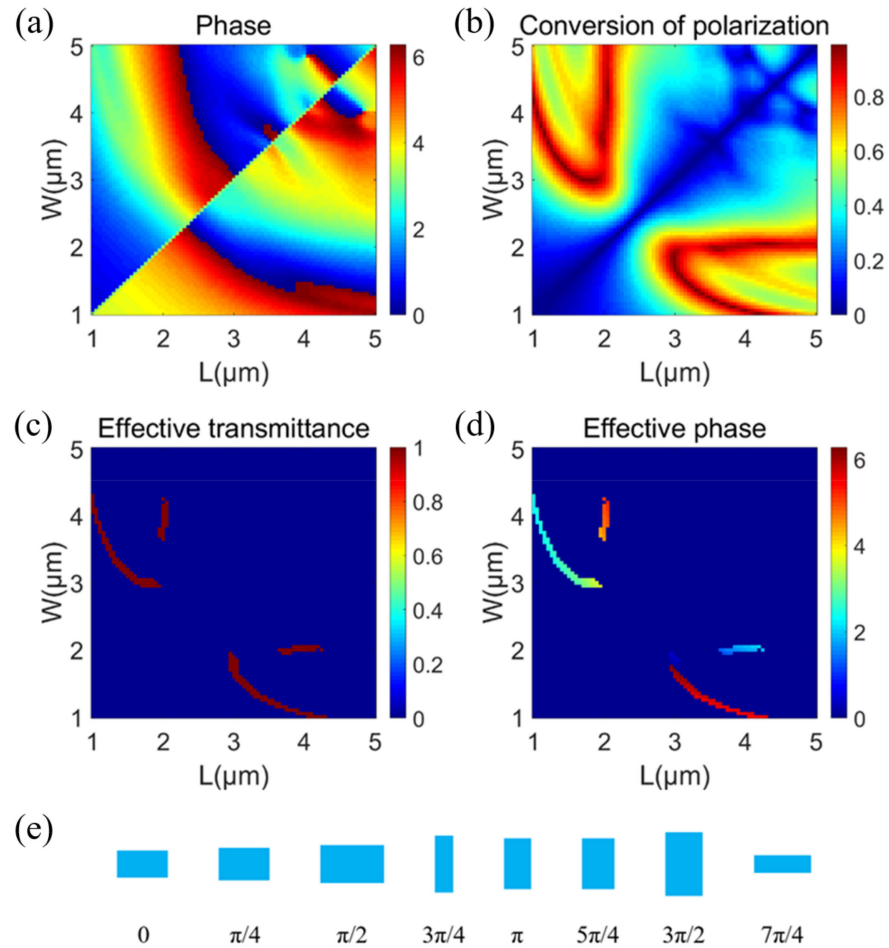


Figure 5. (a) The relationship between the propagation phase and the length and width of the nanorods when the LCP light is the main transmitted light. (b) The conversion rate of polarization when the RCP light is incident. (c,d) The transmission and propagation phase distribution of the unit cells meeting the conditions of transmittance > 0.9 and conversion rate > 0.9. (e) Schematic of the 8 basic unit cell elements.

Finally, the OCPM model is established and simulated. The diameter of the designed metalens is 150 μm , the focal length is 150 μm and the off-axis angle of the focus is 8° . The metalens light sources are set to RCP light, LCP light and 45° linearly polarized light in turn; the normalized distribution of the square of the electric field intensity of the metalenses are shown in Figure 6. RCP light and LCP light both have a focusing efficiency of 60%. The extinction ratio between the two orthogonally polarized channels is 0.20 dB.

2.2. Design of the SAM

The design of SAM mainly includes the following two steps: Firstly, the synthetic aperture array structure is designed. After considering the application requirements of MTF, the number of sub-apertures, circumcircle aperture, filling factor and other parameters are determined. Secondly, the SAM is designed according to the array structure and polarization.

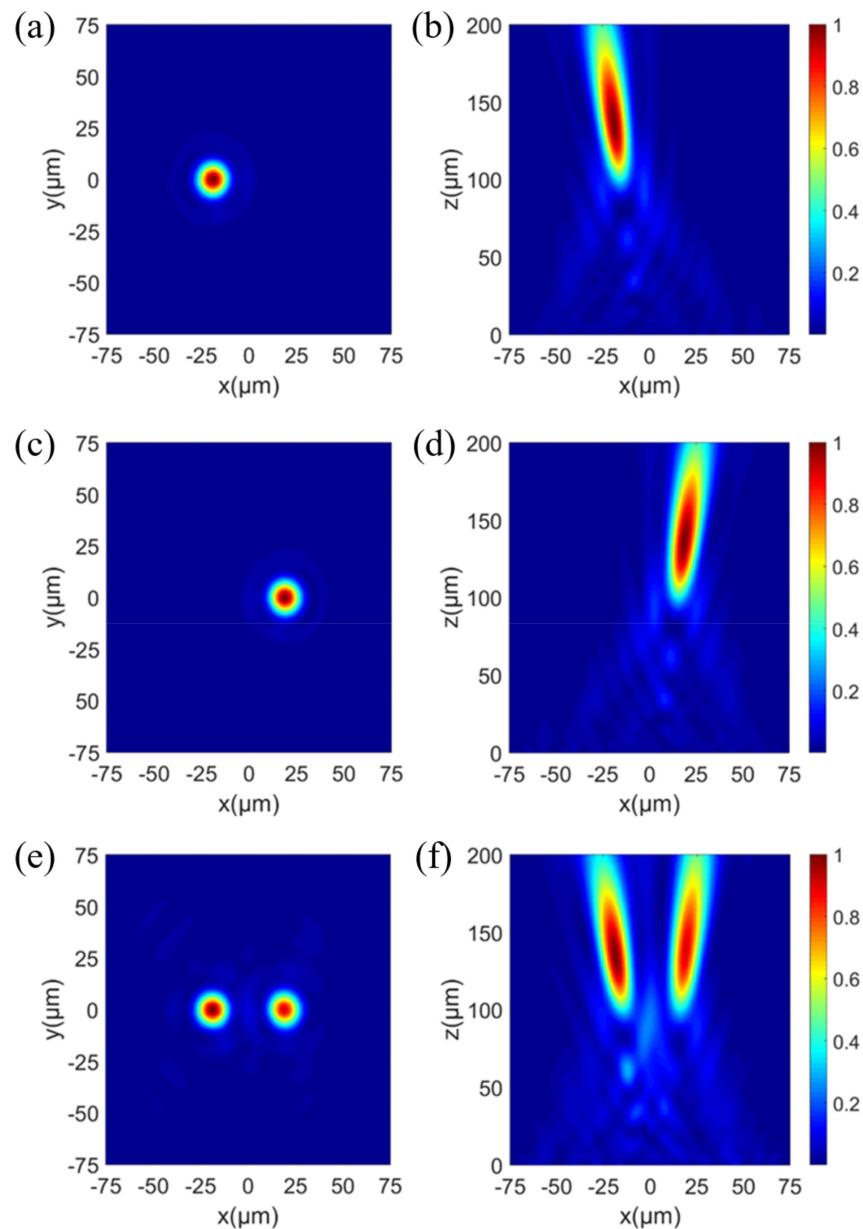


Figure 6. When RCP light, LCP light and 45° linearly polarized light successively pass through the OCPM, the normalized distribution of the square of the electric field intensity: (a,c,e) X–Y plane; (b,d,f) X–Z plane.

The design of the array structure is an important step. The common synthetic aperture structures such as Golay3, Cross and Annulus are analyzed and discussed below. It is assumed that the circumradius of the SAM is 80 mm and the focal length is 350 mm. If the filling factors are all 51%, then the sub-aperture radii of Golay3, Cross and Annulus structures are 33 mm, 23.3 mm and 25.5 mm, respectively. The calculated MTFs of different SAMs are shown below:

It can be seen from Figure 7 that the cutoff frequencies of the three synthetic aperture structures are significantly improved compared with the single-aperture structures. The cutoff frequency of Golay3 structure in the X-axis direction is greater than that in the Y-axis direction. Annulus structure’s cutoff frequencies are opposite. Because the Cross structure is symmetrical in the center, its MTFs in the X-axis and Y-axis directions are the same. The intermediate frequency responses of the three structures are close to 0.2.

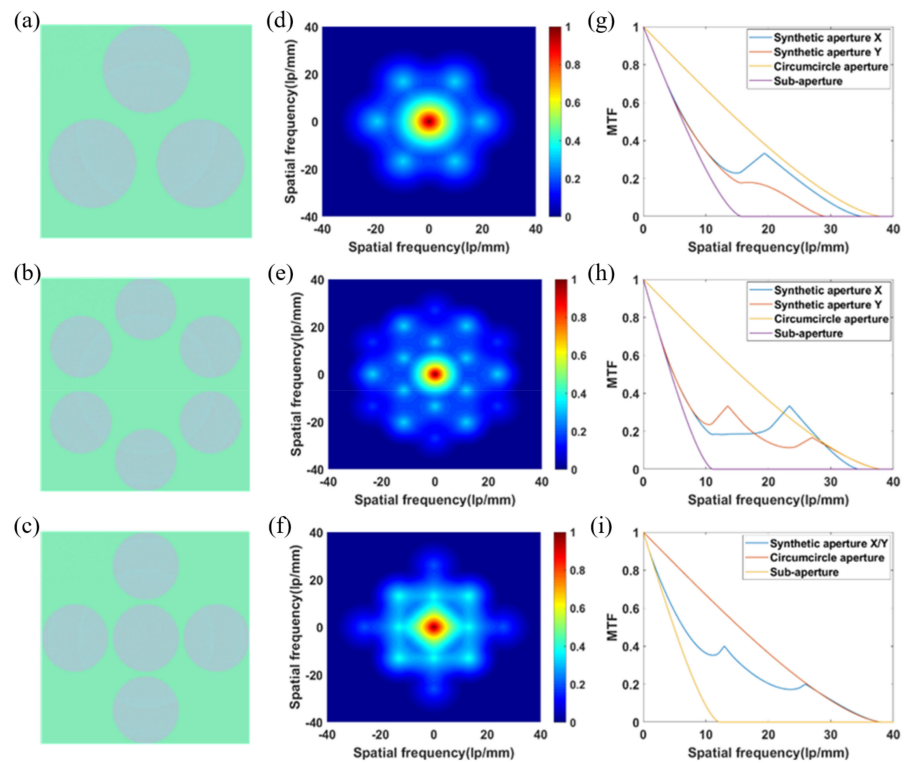


Figure 7. (a–c) Schematic of the SAMs with structures of Golay3, Annulus and Cross, respectively. (d–f) Calculated MTFs of the SAMs. (g–i) MTFs of the SAMs in the X– and Y– axis directions.

It can be seen from Figure 8 that the phase distributions of the SAMs are spatial interceptions of the phase distribution of the full-aperture metalens. For the metalens, with the increase in radius, the phase difference between adjacent periodic elements will increase, and the phase accuracy will be improved. As mentioned above, SAMs are designed to meet the need for large apertures. Therefore, in order to achieve better performance of SAMs, the phase accuracy at different radii should be separately considered during the design process.

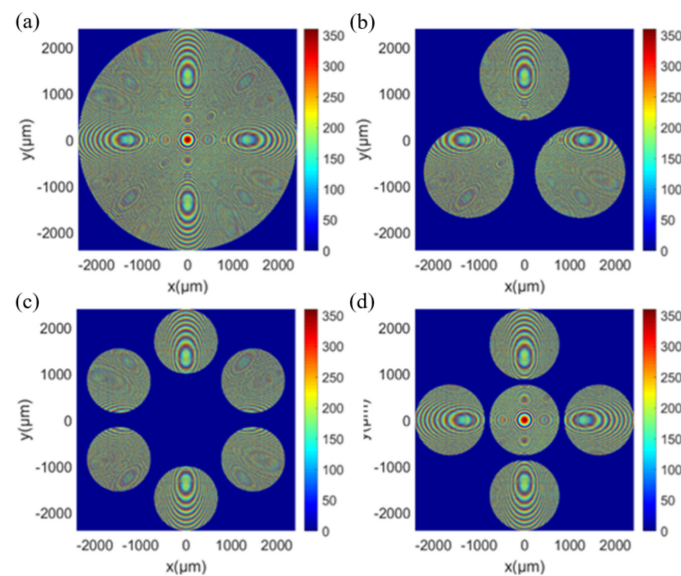


Figure 8. (a–d) The phase distributions of SAMs with structures of the full–aperture, Golay3, Annulus and Cross, respectively.

In addition to the type of synthetic aperture array structure, the filling factor of the array also has a significant effect on the MTF. Taking the Cross structure as an example, the MTFs of synthetic apertures with different filling factors are shown in Figure 9. With the decrease in filling factor, the intermediate-frequency response of the synthetic aperture decreases gradually. More seriously, some array structures may even have a zero response under low filling factor conditions, which is not conducive to obtaining high-quality images. Therefore, a suitable array structure and filling factor should be selected during the design of SAM.

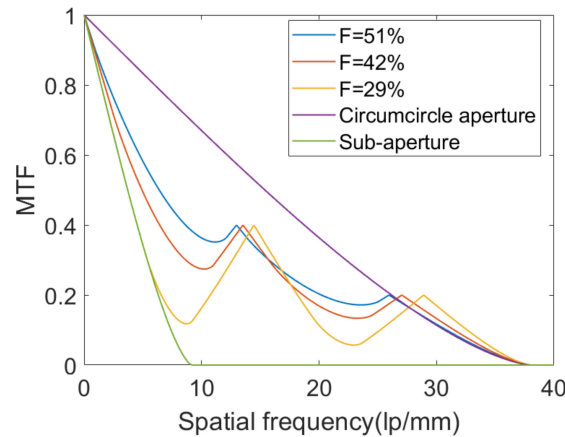


Figure 9. The MTFs corresponding to filling factors are 51%, 42% and 29%, respectively.

The MTF of synthetic aperture in the mid-frequency range is lower than that of the full aperture, which affects the quality of the image. Image restoration algorithms are often used to reduce the impact of intermediate-frequency loss. For example, Wiener filter deconvolution algorithm [32], Lucy–Richardson deconvolution algorithm [33] and maximum likelihood deconvolution algorithm [34]. In order to demonstrate the effect of image restoration algorithm, this paper simulates the imaging processes of three kinds of SAMs with filling factors of 42%. Lucy–Richardson deconvolution algorithm is used to process images directly obtained by SAMs. The corresponding degraded images and restored images are shown in the Figure 10.

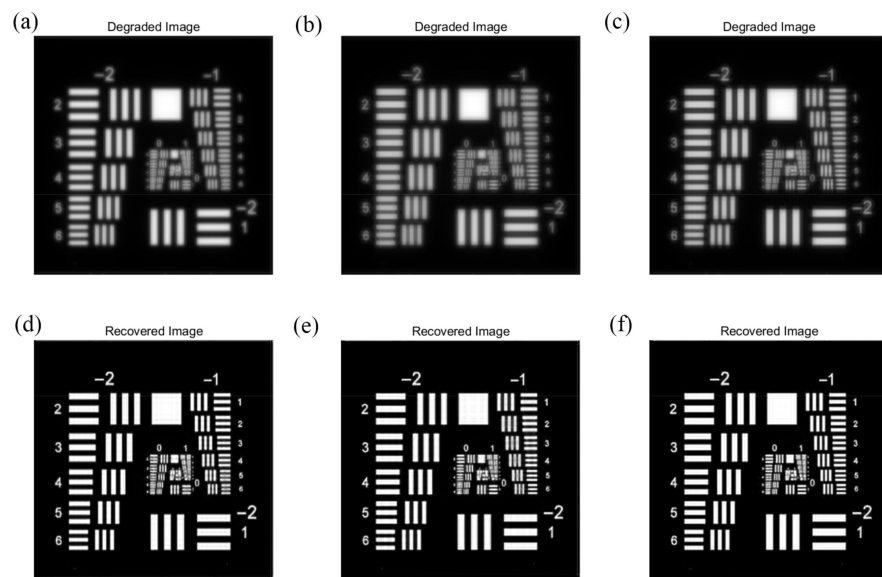


Figure 10. (a–c) The degraded images of the SAMs with structures of Golay3, Annulus and Cross, respectively. (d–f) The recovered images of the SAMs with structures of Golay3, Annulus and Cross, respectively.

Two image quality evaluation indexes, PSNR and SSIM, were used to evaluate the above images. The specific results are shown in the Table 2.

Table 2. The image quality of the corresponding degraded images and restored images.

Array Structures	Degraded Images		Restored Images	
	PSNR	SSIM	PSNR	SSIM
Golay3	16.5	0.49	23.6	0.92
Cross	16.2	0.44	25.7	0.94
Annulus	15.1	0.39	24.3	0.91

By analysis of Figure 10 and Table 2, it can be found that the image restoration algorithm significantly improves the quality of degraded images. Moreover, because the MTF cutoff frequency of the Cross is the largest, its image recovery effect is the best. It is worth emphasizing that the image recovery algorithms can only compensate the intermediate-frequency loss of MTF within certain limits. When the intermediate frequency is too low or zero, the image recovery algorithms are powerless.

3. Results and Discussion

In this chapter, we verify the SAMs through simulation experiments. In order to speed up the simulation, we use the scale-down model. The circumradii of the designed SAMs are 240 μm and the focal lengths are 1050 μm . When the filling factors are all 51%, the point spread functions (PSFs) of polarization-insensitive, orthogonal linearly polarized and orthogonal circularly polarized SAMs are shown in Figure 11. The extinction ratio between the two orthogonally polarized channels of OLP-SAMs with array structures of Golay3, Cross and Annulus are 0.12 dB, 0.20 dB and 0.15 dB. As for OCP-SAMs, they are 0.10 dB, 0.47 dB and 0.31 dB, respectively.

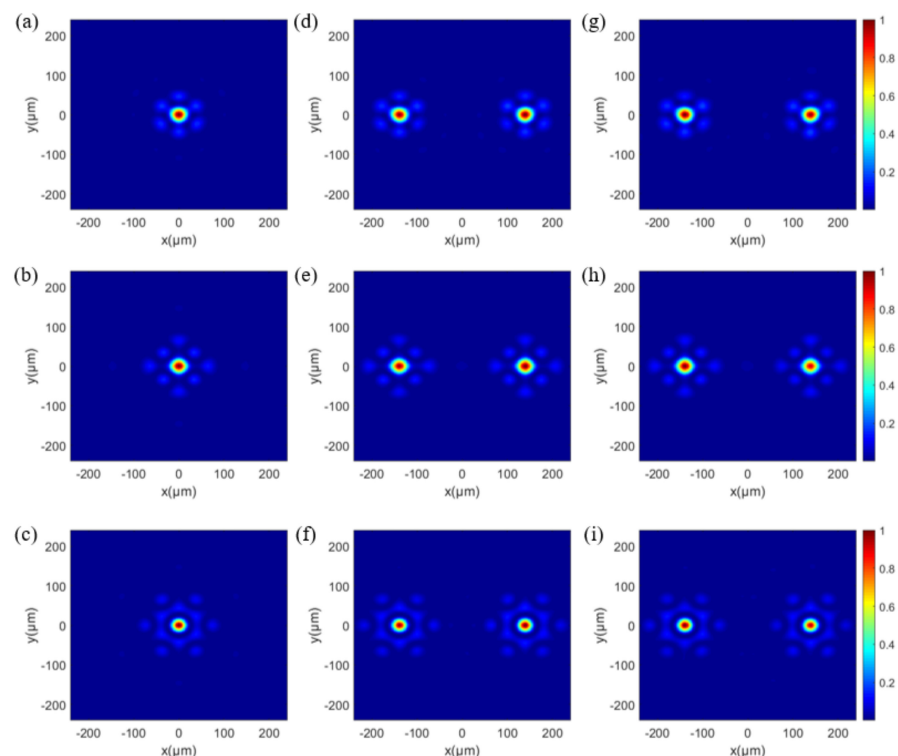


Figure 11. (a–c) The PSFs of PI-SAMs with structures of Golay3, Cross and Annulus, respectively. (d–f) The PSFs of OLP-SAMs with structures of Golay3, Cross and Annulus, respectively. (g–i) The PSFs of OCP-SAMs with structures of Golay3, Cross and Annulus, respectively.

When the circumradii and focal lengths of the SAMs stay the same, the synthetic aperture structures and filling factors change, respectively; the simulation results of the SAMs are shown in Table 3.

It can be seen from Table 3 that:

As the filling factor increases gradually, the focusing efficiency also increases. This is mainly because with the increase in filling factor, the number of nanorods in the SAM increases, so that more energy is focused at the focal point, thus increasing the focusing efficiency of the SAM. In addition, the cutoff frequency of the SAM can be improved by increasing the filling factor.

When the filling factors are the same, Golay3 has the highest focusing efficiency, Cross has the lower focusing efficiency and Annulus has the lowest focusing efficiency. This is mainly because with the increase in the metalens's radius, the phase change is accelerated, resulting in the increase in phase error, so the focusing efficiency is reduced. Therefore, when designing SAMs, array structures such as Annulus, where the effective region is far from the center, should not be adopted. At the same time, considering MTF, we suggest using a structure such as Cross, which has high cutoff frequency, intermediate frequency response and focusing efficiency.

For SAMs with different polarization types, the focusing efficiencies of polarization-insensitive SAMs are higher, and those of orthotropic linear polarization and orthotropic circular polarization SAMs are lower. This is mainly due to the minimum phase error of polarization-insensitive SAMs. Because the phase errors of OLP-SAMs are different for X-polarization and Y-polarization, the focusing efficiencies of the two polarized lights are different. In addition to phase errors, the low focusing efficiencies of OCP-SAMs are due to the effect of conversion less than 1.

Table 3. The focusing efficiency of different SAMs.

Array Structures	Filling Factors	PI-SAM	OLP-SAM		OCP-SAM	
Golay3	29%	24%	22%	23%	22%	23%
	42%	42%	39%	32%	40%	41%
	51%	48%	44%	46%	47%	47%
Cross	29%	24%	20%	18%	22%	22%
	42%	33%	31%	32%	33%	33%
	51%	41%	38%	39%	42%	42%
Annulus	29%	17%	15%	15%	15%	15%
	42%	27%	23%	23%	23%	23%
	51%	30%	28%	29%	29%	29%

4. Conclusions

In summary, we design and simulate the polarization-insensitive, orthogonal linearly polarized and orthogonal circularly polarized SAMs. Two orthogonal polarized lights can be focused separately in the same aperture of the metalens, which improves the energy utilization and the system integration compared with the traditional polarization system. We studied the common array structures of SAMs such as Golay3, Cross and Annulus, and compared the MTF and focusing efficiency of different array structures of SAMs. Through this research, we use a synthetic aperture to improve the cutoff frequency of the metalens and achieve the equivalent large-aperture metalens. This paper provides an effective solution to the needs of large-aperture metalenses, and metalenses with different polarizations can play an important role in polarization imaging.

Author Contributions: The listed authors' contributions to this work are as follows: Conceptualization, J.H. and Z.D.; methodology, J.H.; software, J.H.; validation, J.H., X.Y. and X.C.; formal analysis, L.X.; investigation, J.H.; resources, L.X.; data curation, Y.L.; writing—original draft preparation, J.H.; writing—review and editing, X.C.; visualization, J.H.; supervision, Z.D.; project administration, Z.D. and L.X. All authors have read and agreed to the published version of the manuscript.

Funding: This research received no external funding.

Institutional Review Board Statement: Not applicable.

Informed Consent Statement: Not applicable.

Data Availability Statement: The data presented in this study are available from the corresponding author upon reasonable request.

Conflicts of Interest: The authors declare no conflict of interest.

References

1. Yu, N.; Capasso, F. Flat optics with designer metasurfaces. *Nat. Mater.* **2014**, *13*, 139–150. [[CrossRef](#)] [[PubMed](#)]
2. Mueller, J.P.B.; Rubin, N.A.; Devlin, R.C.; Groever, B.; Capasso, F. Metasurface Polarization Optics: Independent Phase Control of Arbitrary Orthogonal States of Polarization. *Phys. Rev. Lett.* **2017**, *118*, 113901. [[CrossRef](#)] [[PubMed](#)]
3. Byrnes, S.J.; Lenef, A.; Aieta, F.; Capasso, F. Designing large, high-efficiency, high-numerical-aperture, transmissive meta-lenses for visible light. *Opt. Express* **2016**, *24*, 5110–5124. [[CrossRef](#)] [[PubMed](#)]
4. Shan, D.; Xu, N.; Gao, J.; Song, N.; Liu, H.; Tang, Y.; Feng, X.; Wang, Y.; Zhao, Y.; Chen, X.; et al. Design of the all-silicon long-wavelength infrared achromatic metalens based on deep silicon etching. *Opt. Express* **2022**, *30*, 13616–13629. [[CrossRef](#)]
5. Chen, W.T.; Zhu, A.Y.; Sanjeev, V.; Khorasaninejad, M.; Shi, Z.; Lee, E.; Capasso, F. A broadband achromatic metalens for focusing and imaging in the visible. *Nat. Nanotech.* **2018**, *13*, 220–226. [[CrossRef](#)]
6. Taghvaei, H.; Liu, F.; Díaz-Rubio, A.; Tretyakov, S. Subwavelength focusing by engineered power-flow conformal metamirrors. *Phys. Rev. B* **2021**, *104*, 235409. [[CrossRef](#)]
7. Lin, C.H.; Chen, Y.S.; Lin, J.T.; Wu, H.C.; Kuo, H.T.; Lin, C.F.; Chen, P.; Wu, P.C. Automatic Inverse Design of High-Performance Beam-Steering Metasurfaces via Genetic-type Tree Optimization. *Nano. Lett.* **2021**, *21*, 4981–4989. [[CrossRef](#)] [[PubMed](#)]
8. Zheng, G.X.; Mühlenbernd, H.; Kenney, M.; Li, G.; Zentgraf, T.; Zhang, S. Metasurface holograms reaching 80% efficiency. *Nat. Nanotech.* **2015**, *10*, 308–312. [[CrossRef](#)] [[PubMed](#)]
9. Wan, W.W.; Gao, J.; Yang, X.D. Full-Color Plasmonic Metasurface Holograms. *ACS Nano* **2016**, *10*, 10671–10680. [[CrossRef](#)]
10. Khorasaninejad, M.; Capasso, F. Metalenses: Versatile multifunctional photonic components. *Science* **2017**, *358*, eaam8100. [[CrossRef](#)]
11. Tan, S.; Yang, F.; Boominathan, V.; Veeraraghavan, A.; Naik, G.V. 3D Imaging Using Extreme Dispersion in Optical Metasurfaces. *ACS Photonics* **2021**, *8*, 1421–1429. [[CrossRef](#)]
12. Sun, T.; Hu, J.P.; Zhu, X.J.; Xu, F.; Wang, C.H. Broadband Single-Chip Full Stokes Polarization-Spectral Imaging Based on All-Dielectric Spatial Multiplexing Metalens. *Las. Phot. Rev.* **2022**, *16*, 2100650. [[CrossRef](#)]
13. Zhu, X.Z.; Cheng, Y.Z.; Chen, F.; Luo, H.; Ling, W. Efficiency adjustable terahertz circular polarization anomalous refraction and planar focusing based on a bi-layered complementary Z-shaped graphene metasurface. *J. Opt. Soc. Am. B* **2022**, *39*, 705–712. [[CrossRef](#)]
14. Yang, D.R.; Cheng, Y.Z.; Chen, F.; Luo, H.; Wu, L. Efficiency tunable broadband terahertz graphene metasurface for circular polarization anomalous reflection and plane focusing effect. *Dia. Rel. Mater.* **2023**, *131*, 109605. [[CrossRef](#)]
15. Wang, S.M.; Wu, P.C.; Su, V.C.; Lai, Y.C.; Chu, C.H.; Chen, J.W.; Lu, S.H.; Chen, J.; Xu, B.B.; Kuan, C.H.; et al. Broadband achromatic optical metasurface devices. *Nat. Commun.* **2017**, *8*, 187. [[CrossRef](#)] [[PubMed](#)]
16. Yao, Y.H.; Liu, H.; Wang, Y.F.; Li, Y.R.; Song, B.X.; Wang, R.P.; Povinelli, M.L.; Wu, W. Nanoimprint-defined, large-area metasurfaces for unidirectional optical transmission with superior extinction in the visible-to-infrared range. *Opt. Express* **2016**, *24*, 15362–15372. [[CrossRef](#)]
17. Park, J.S.; Zhang, S.Y.; She, A.; Chen, W.T.; Lin, P.; Yousef, K.M.A.; Cheng, J.X.; Capasso, F. All-glass, large metalens at visible wavelength using deep-ultraviolet projection lithography. *Nano Lett.* **2019**, *19*, 8673–8682. [[CrossRef](#)]
18. Balli, F.; Sultan, M.A.; Ozdemir, A.; Hastings, J.T. An ultrabroadband 3D achromatic metalens. *Nanophotonics* **2021**, *10*, 1259–1264. [[CrossRef](#)]
19. Li, J.W.; Wang, Y.L.; Liu, S.J.; Xu, T.; Wei, K.; Zhang, Y.D.; Cui, H. Largest aperture metalens of high numerical aperture and polarization independence for long-wavelength infrared imaging. *Opt. Express* **2022**, *30*, 28882–28891. [[CrossRef](#)]
20. Zhao, F.; Shen, Z.C.; Wang, D.C.; Xu, B.J.; Chen, X.N.; Yang, Y.M. Synthetic aperture metalens. *Photonics Res.* **2021**, *9*, 2388–2397. [[CrossRef](#)]
21. Wang, D.Y.; Han, J.; Liu, H.C.; Tao, S.Q.; Fu, X.Y.; Guo, H.F. Experimental study on imaging and image restoration of optical sparse aperture systems. *Opt. Eng.* **2007**, *46*, 103201. [[CrossRef](#)]

22. Sabatke, E.M.; Burge, J.H. Basic principles in the optical design of imaging multiple aperture systems. *Proc. SPIE* **2002**, *4832*, 236–248.
23. Garcia, N.M.; Erausquin, I.D.; Edmiston, C.; Gruev, V. Surface normal reconstruction using circularly polarized light. *Opt. Express* **2015**, *23*, 14391–14406. [[CrossRef](#)] [[PubMed](#)]
24. Zhang, W.F.; Liang, J.; Ren, L.Y.; Ju, H.J.; Qu, E.S.; Bai, Z.F.; Tang, Y.; Wu, Z.X. Real-time image haze removal using an aperture-division polarimetric camera. *Appl. Opt.* **2017**, *56*, 942–947. [[CrossRef](#)] [[PubMed](#)]
25. Jin, H.H.; Qian, L.J.; Gao, J.; Fan, Z.G.; Chen, J. Polarimetric calculation method of global pixel for underwater image restoration. *IEEE Photonics J.* **2021**, *13*, 1–15. [[CrossRef](#)]
26. Wu, R.Y.; Zhao, Y.Q.; Li, N.; Kong, S.G. Polarization image demosaicking using polarization channel difference prior. *Opt. Express* **2021**, *29*, 22066–22079. [[CrossRef](#)]
27. Morel, O.; Meriaudeau, F.; Stolz, C. Polarization imaging applied to 3D reconstruction of specular metallic surfaces. *Proc. SPIE* **2005**, *5679*, 178–186.
28. Arbabi, E.; Kamali, S.M.; Arbabi, A.; Faraon, A. Full Stokes imaging polarimetry using dielectric metasurfaces. *ACS Photonics* **2018**, *5*, 3132–3140. [[CrossRef](#)]
29. Wang, S.; Wang, X.K.; Kan, Q.; Ye, J.S.; Feng, S.F.; Sun, W.F.; Han, P.; Qu, S.L.; Zhang, Y. Spin-selected focusing and imaging based on metasurface lens. *Opt. Express* **2015**, *23*, 26434–26441. [[CrossRef](#)]
30. Chen, S.Q.; Li, Z.; Zhang, Y.B.; Cheng, H.; Tian, J.G. Phase Manipulation of Electromagnetic Waves with Metasurfaces and Its Applications in Nanophotonics. *Adv. Optical Mater.* **2018**, *6*, 1800104. [[CrossRef](#)]
31. Li, X.S.; Chen, S.Q.; Wang, D.; Shi, X.T.; Fan, Z.G. Transmissive mid-infrared achromatic bifocal metalens with polarization sensitivity. *Opt. Express* **2021**, *29*, 17173–17182. [[CrossRef](#)] [[PubMed](#)]
32. Gonzalez, R.C.; Woods, R.E. *Digital Image Processing*; Addison-Wesley Publishing Company, Inc.: Reading, MA, USA, 1992.
33. Biggs, D.S.C.; Andrews, M. Acceleration of iterative image restoration algorithms. *Appl. Opt.* **1997**, *36*, 8. [[CrossRef](#)] [[PubMed](#)]
34. Holmes, T.J.; Bhattacharyya, S.; Cooper, J.A.; Hanzel, D.; Turner, J.N. Light Microscopic Images Reconstructed by Maximum Likelihood Deconvolution. In *Handbook of Biological Confocal Microscopy*; Pawley, J.B., Ed.; Plenum Press: New York, NY, USA, 1995.

Disclaimer/Publisher’s Note: The statements, opinions and data contained in all publications are solely those of the individual author(s) and contributor(s) and not of MDPI and/or the editor(s). MDPI and/or the editor(s) disclaim responsibility for any injury to people or property resulting from any ideas, methods, instructions or products referred to in the content.